High-flux sublimation of a 3D carbon/carbon composite: surface roughness patterns

Cyril Levet[a,b], Jean Lachaud[c], Virginie Ducamp[b], Régis Memes[b],
Jacques Couzi[b], Julien Mathiaud[b], Adrien P. Gillard[a,b], P. Weisbecker[a],
Gérard L. Vignoles[a,*]

[a]*University of Bordeaux, LCTS, 3 Allée de la Boétie, F-33600 Pessac, France*
[b]*CEA,CESTA, 15 Avenue des Sablières, F-33114 Le Barp, France*
[c]*Université de Bordeaux, I2M – Dept. TREFLE – Site ENSAM, Esplanade des Arts et Métiers,
F-33400 Talence, France*

Abstract

3D carbon-fibre reinforced carbon composites (3D C_f/C) are used as thermal protection systems for atmospheric re-entry, where they are exposed to strong ablation. Particularly, sublimation of the carbonaceous material plays an important role during the re entry. To study this, an arc image furnace under controlled Argon flow is used, with heat fluxes of $8\,\mathrm{MW\,m^{-2}}$ to $10\,\mathrm{MW\,m^{-2}}$. The furnace and the sample thermal response have been numerically simulated prior to the experiments and match in-situ temperature measurements. Scanning electron microscopy and 3D profilometry with digital optical microscopy were used in order to characterise the epi-macro-structural and the epi-micro-structural roughness of the composite surface, evidencing a faster recession of the fibres as compared to the matrix. Carbon nanotextures have been assessed by using High-Resolution Transmission Electron Microscopy and Polarised Light Optical Microscopy, showing that the matrix is more organised than the fibre. This can ex-

*Corresponding author. E-mail: vinhola@lcts.u-bordeaux.fr

plain the "inverse" behaviour under sublimation as compared to oxidation. The results have been qualitatively interpreted using numerical simulation of differential surface recession.

Highlights

- 3D C_f/C composites were submitted to fluxes of $8\,\mathrm{MW\,m^{-2}}$ to $10\,\mathrm{MW\,m^{-2}}$ under Ar atmosphere in an image furnace at pressures of $1\,\mathrm{kPa}$ to $10\,\mathrm{kPa}$.

- The surfaces were investigated by SEM and show a very specific roughness morphology.

- The fibre recedes faster than the matrix, as opposed to oxidation tests.

- Ablation modelling confirms that:

  1. the fibre is more sensitive to sublimation than the matrix and,

  2. diffusion of sublimation products is not a limiting phenomenon.

- The degree of organization of the carbon-based constituents has a positive impact on the recession rate.

1. Introduction

Carbon-fibre reinforced carbon composites (CFRC or C_f/C for short) are dedicated to high-flux applications where thermal and structural strength are a vital requirement [1]. They are used as Thermal Protection Material (TPM) in various applications such as atmospheric re-entry [2–4], solid rocket motor [5–7] (SRM), aircraft braking system [8] and plasma facing elements of the Tokamak [9, 10]. However, because they are composed of graphitic carbon, these materials are oxidized above $800\,\mathrm{K}$. At higher temperatures, they undergo nitridation if atomic

2

nitrogen is present [11] and finally start sublimating at $\approx 2700\,$K. Moreover, mechanical erosion can occur in high speed flow. These phenomena are collected under the generic term of ablation. If oxidation is an exothermic phenomenon, sublimation is endothermic : it transforms the thermal energy into mass loss and surface recession, whilst the remaining solid insulates the vehicle body [12]. That is why ablation is globally endothermic for very high temperatures, when sublimation is the main phenomenon.

Ablation of C_f/C composite is known to lead, among others, to a typical surface roughness [13–16] which affects the laminar-to-turbulent transition inside the boundary layer [17, 18]. Selection and thickness definition of the TPM are then key parameters in Thermal Protection System (TPS) design. Therefore, the understanding of the interaction between the material and his close environment has to be well known for all these applications.

If surface recession of C_f/C in the oxidation regime has been extensively studied [19–23], it is not the case for the sublimation regime, probably due to the extremely high temperatures and heat fluxes necessary for such a study. The first studies on TPM sublimation [24, 25] focus on graphites. Lundell and Dickey [26] have only reported on mass loss rates, not on surface morphology. Farhan *et al.* [27] have shown that, when switching progressively from air to argon in a plasma jet, the surface temperature increases but the recession rate diminishes, as well as the sample epi-macrostructural roughness, but no detail on the surface features are provided. These studies have shown that, because the testing conditions include high-velocity gas or plasma streams, mechanical erosion plays a non-negligible role. If one wants to fully decouple mechanical erosion from sublimation in very high heat flux experiments, another type of set-up has to be involved. Arc image

3

furnace are radiation heating devices that can deliver high heat-flux. Such a high temperature experimental set-up with controlled flow is very useful for TPM qualification and TPS design. Some of us [12] have reported that fibre recession under sublimation is faster than matrix recession, as opposed to oxidation cases, but this fact has never been fully explained.

In this work, we report new data on 3D C_f/C composites ablation under an argon flow to improve the understanding of this material behaviour during atmospheric re-entry. The arc image furnace used here can produce heat fluxes from $1\,\mathrm{MW\,m^{-2}}$ to $30\,\mathrm{MW\,m^{-2}}$ under reduced pressure ($P < 1\ bar$) and a controlled argon flow [28]. A numerical simulation has been used to reconstruct the flow field in the furnace. Flat cylindrical samples were tested at pressures of 0.01 bar - 0.1 bar and heat flux from $8\,\mathrm{MW\,m^{-2}}$ to $10\,\mathrm{MW\,m^{-2}}$. Characterisation of the fibres and the surrounding matrix was made by scanning and transmission electron microscopy and polarised light optical microscopy. Experimental results were interpreted with the help of a surface recession simulation code [29].

2. Experiments

2.1. Test material

The sample material was a 3D C_f/C composite made from ex-PolyAcryloNitrile (PAN) carbon fibres and ex-pitch carbon matrix [16, 30]. Several thousands of fibres (3 to 12,000) are linked together by a pitch-based matrix in a straight, unidirectional yarn, named "bundle". Then, fibre bundles are fit together into a 3D orthogonal pattern repeated by translation of a cubic lattice. This leads to a network of parallelepipedic void spaces. They are partially filled with a pitch-based carbon matrix and will be called "matrix pockets". Finally, the composite is highly graphitised.

Samples were cylinders of 1 cm diameter and 1 cm height. They were embedded in a *Calcarb®* rectangular cuboid sample holder which was 10 cm wide and 3 cm deep (Figure 1). In the rest of the document, bundles perpendicular to the surface – *ie.* in z direction –, will be called "vertical", the other ones – *ie.* in x or y directions – being called "horizontal".
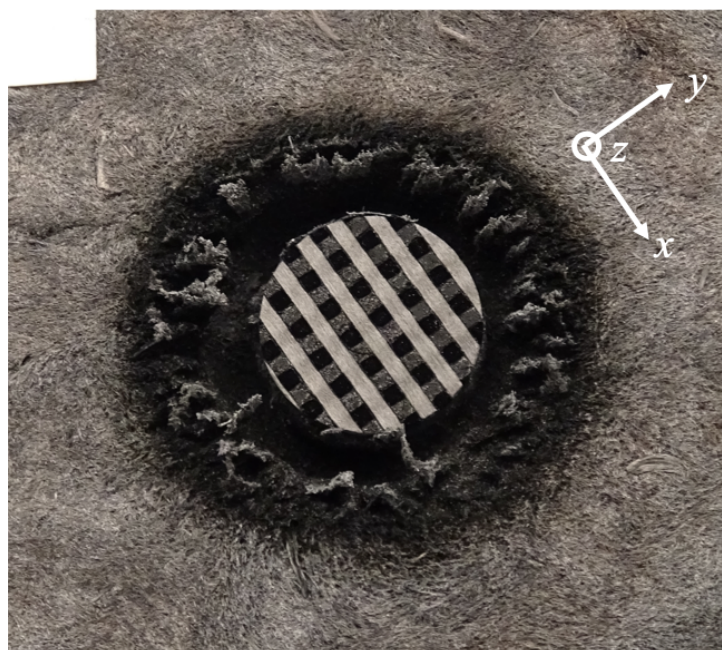

Figure 1: Photograph of a sample and its sample holder after a sublimation test in the arc image furnace

2.2. The high-flux image furnace

An arc image furnace equipped with six 7 MW Xenon lamps has been used in these experiments [28]. The sample is enclosed in a cooled cubic chamber with a quartz window allowing its heating by radiative transfer (Figure 2). The sample holder assembly is bound to a metal backing. An argon flow is injected in the furnace chamber through a tubular injection device placed just below the sample.

5

Gases are ejected through an aspiration system located on one of the lateral walls of the furnace. Pressure is measured by a Brooks CMC 100 mbar pressure gauge. A Brooks SLA5850 - 1000 sccm flowmeter coupled to an ASC pressure regulator and two WEST 8800 process controllers regulate the flow rate in the chamber. The vacuum is ensured by an Alcatel 21L vacuum pump.

The test conditions for material sublimation are summarised in table 1. Six different tests were conducted. In the *Reference* test, the sample was equipped with a thermocouple in order to compare with simulations (section 3.2). The static pressure varied from 10 mbar to 100 mbar and the argon flow was 100 cm^3 min^{-1} or 1000 cm^3 min^{-1}. The selected heat flux was 8 MW m^{-2} or 10 MW m^{-2}. The test time was 30 s for all tests except one which only lasts 15 s in order to explore the transient regime. The two pressures were selected to investigate pressure effect on 3D C_f/C sublimation rate. The different flow rates are chosen to explore their impact on the composite surface roughness.

The *Reference* test was conducted to match conditions of a previous investigation [12], the *Mean pressure* and *High pressure* tests were designed to explore the effect of pressure whereas the *Minimal sublimation* test was to quantify the influence of the heat flux on surface recession. *Low flow rate* was used to show the impact of the flow on the surface roughness. Lastly, the *Transient* test was made to examine the transient regime of sublimation.

2.3. Diagnostics

Before running the experiment, a calorimeter is placed in the chamber in order to adjust the lamp focus and the position of the sample because the settings have to be changed for each desired heat flux. The pressure, argon flow rate and lamp power supply are recorded during the whole experiment. The static pressure
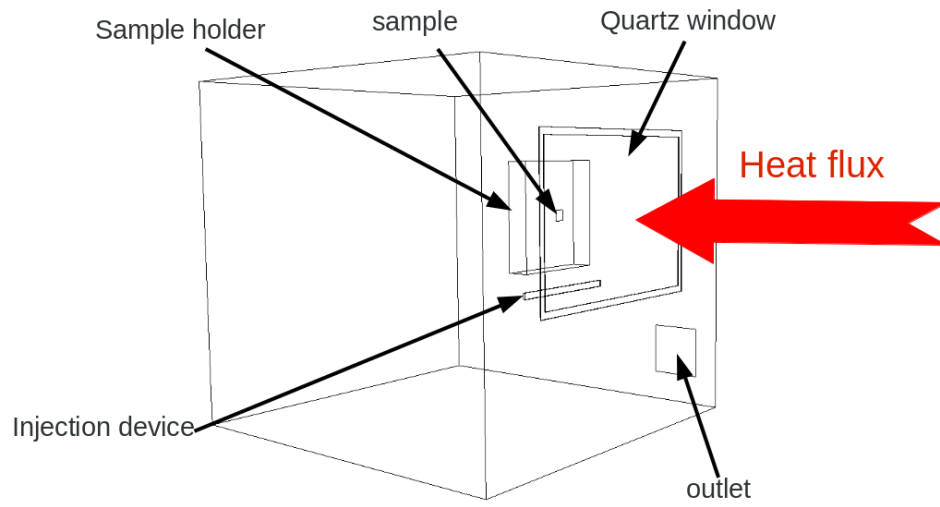
(a) Furnace scheme
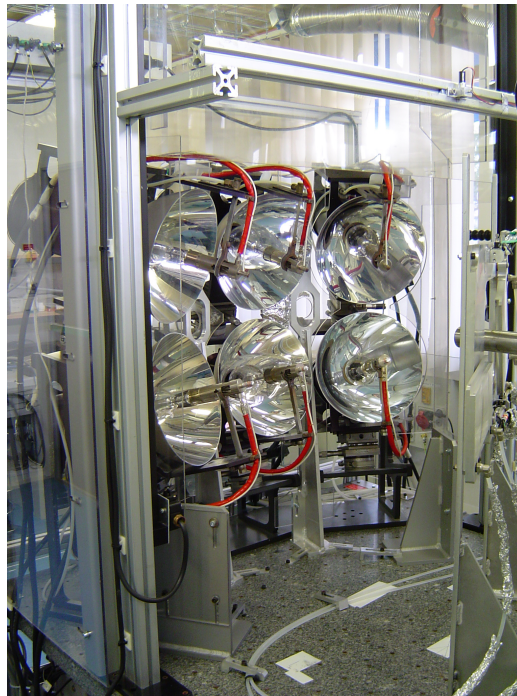
(b) Xenon lamps

Figure 2: a) Scheme of the arc image furnace chamber and b) picture of the six Xenon lamps

Sample	p_s (bar)	ϕ_q (MW m^{-2})	τ (s)	Q (cm^3 min^{-1})
Reference	0.01	10	30	1000
Minimal sublimation	0.1	8	30	1000
Mean Pressure	0.05	10	30	1000
High Pressure	0.1	10	30	1000
Low flow rate	0.01	10	30	100
Transient	0.01	10	15	1000

Table 1: Arc image furnace test conditions : test case name, static pressure p_s, cold wall heat flux ϕ_q, sample exposure time τ, and gas flow rate Q

and the argon flow on the sample were continuously monitored by the pressure gauge and the flowmeter. One of the samples was instrumented with a type C thermocouple placed 3 mm from the rear side. Type C thermocouples are generally considered fully reliable up to 2200 °C but can provide measurements for temperatures up to 2800 °C in favourable cases. In most experiments, the thermocouple was oriented perpendicular to the stream lines. However, we also have tested the other orientation of the thermocouple without noticing any large temperature difference.

2.4. Thermal & Computational Fluid Dynamics (CFD) tools

Before running the experiments, it is necessary to verify correct operating conditions for the setup: (*i*) absence of hot gases at the outlet, (*ii*) the flow close to the wall is not perturbed by the gas injection close to the window. Moreover, it is important to bring confidence to the measurement of the high temperature of the surface, ensuring that sublimation conditions are reached. So, ~~In order to identify the local conditions in which the sublimation takes place,~~ a simulation of the sample and of the flow field around it in the arc image furnace has been carried out. First, the heating of the sample holder assembly is simulated using *Open-*

FOAM[1]. This software solves the transient heat equation by the Finite Volumes method. A perfect contact between materials has been assumed. The heating flux is taken constant on the sample and zero elsewhere. Solid surfaces are considered to exchange heat only by radiation and the cooling by sublimation is neglected. Material characteristics are presented in table 2. Data for sample thermal properties are taken at 3000 K [1]. Characteristics for the *Calcarb*® sample holder come from the manufacturer[2]. All properties are considered independent of temperature which is a sufficient approximation for our purpose.

	Sample	*Sample holder*
ρ_s (kg m^{-3})	1960	180
C_p (J K^{-1})	2200	2200
λ_s (W m^{-1} K^{-1})	35	1
α (mm^2 s^{-1})	8.1	2.5

Table 2: Sample and sample holder thermal characteristics : density ρ_s, heat capacity C_p, thermal conductivity λ_s and thermal diffusivity α

A complete simulation of the flow field in the arc image furnace has also been carried out using *OpenFOAM*. The interaction between the fluid, the solid and the internal geometry of the furnace are rather complex to simulate. The following simplifying assumptions have been made :

- weak coupling between fluid and solid : a transient calculation of the solid heating is performed; then, the final results are injected in a steady state calculation of the flow ;

- the metal support of the sample holder is not taken into account ;

---

[1]http://openfoam.org/(consulted July 8, 2020)

[2]https://www.mersen.com/products/graphite-specialties/carbon-insulation/rigid-carbon-insulation. (consulted July 8, 2020)

- the tubular injection device is modelled by a slit with an equivalent flow rate.

- the thermophysical properties of the materials have been averaged over the temperature interval of interest and held constant.

Laminar, compressible Navier-Stokes equations with gravity are used for the flow part. The fluid is a perfect gas of pure Argon with constant properties. Heat transfer by radiation is neglected in the fluid simulation, *i.e.* the fluid is considered transparent. The temperature on the faces of the sample holder assembly is injected as a boundary condition in the simulation and the fluxes at the same faces are the output data which are used in the solid calculation. When the variation of the fluxes is less than 0.01 %, the simulation is deemed converged. It takes between 3 and 13 iterations to reach this criterion.

2.5. *Material analyses*

Material characterisation was performed by Scanning Electron Microscopy (SEM), by 3D optical microscopy, by High-Resolution Transmission Electron Microscopy (HRTEM) and by polarised light optical microscopy (PLOM).
The SEM system used in this study was a Hitachi S4500 FEG. The accelerating voltage was 3 kV and the working distance was about 15 mm.
The 3D optical microscope is a Keyence VHX-2000. Its large depth of field allows a 3D reconstruction of the sample surface and therefore gives access to composite roughness measurement. Two objectives were used : a ×20 - ×200 and a ×100 - ×1000.
TEM analyses are carried out with a Philips CM30ST device (LaB_6, operated at

300 kV) with a point resolution of 0.2 nm. HRTEM images are obtained on the thinner parts of thin slices with a 30 mm diameter objective diaphragm. Samples for TEM observations are prepared by first cutting coatings in transversal sections, and then reducing slices to 120 mm by mechanical polishing using a 15 mm diamond plate. The JEOL Ion Slicer (EM-09100IS) device is used for Ar^+ ion milling performed using an incident energy of 5.5 kV and incident angles of 0.5° until 2 h and 2.5° until perforation occurs in the specimen. Thin slices are then decontaminated at 2 kV during 10 min.

The optical microscope was a Nikon ME500L working in reflection mode. It is equipped with a Nikon digital camera DMX 1200 which converts linearly the intensity to an 8-bit grayscale value. It is also equipped with a graduated polariser and analyser. This set-up has been previously fully validated for the analysis of anisotropy of carbonaceous materials [31].

3. Results

3.1. Characterizations of the carbon nanotextures

Figure 3 presents optical micrograph processed by analysis of polarised light and TEM view of vertical fibres (*ie.* in z direction, see fig. 1). In these PLOM images, the brightness level is an indication of the level of anisotropy of carbon while the colour indicates the local anisotropy axis orientation [31]. The inter-fibre matrix is brighter than the fibre which indicates a more organised carbon. On HRTEM pictures (Figure 3 c), d) and e)) it is clear that the matrix is more organised than carbon fibres. Due to fabrication process graphene planes are shorter in the fibre compared to matrix ones. That leads to a less organised and less dense carbon fibre compared to its surrounding matrix.
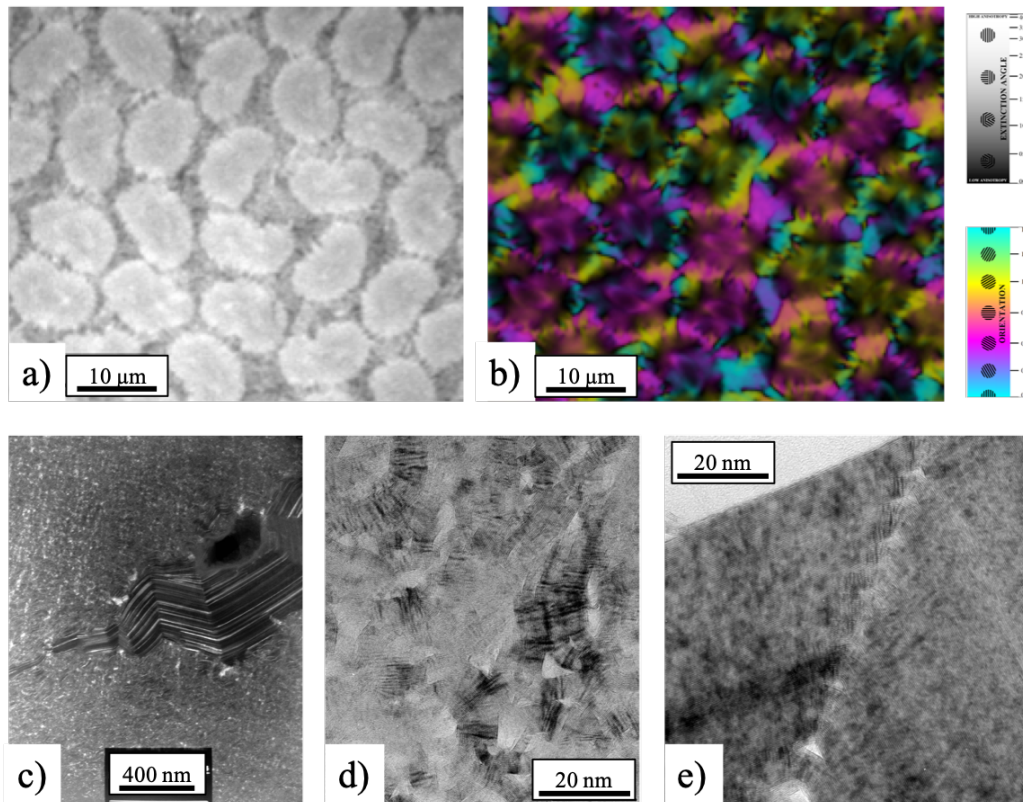
Figure 3: Nanotexture of the carbon fibres and matrix in a bundle. a) Optical micrograph showing fibres and matrix. b) same area processed by analysis of polarised light with analyser/polariser rotations. The brightness level is a quantification of the degree of anisotropy and the colour gives the local direction of anisotropy. c) TEM view of a matrix zone between two fibres. d) HRTEM view of the interior of a fibre. e) HRTEM view of a matrix zone containing a kink.

3.2. Thermal & CFD analysis of the experiments

3.2.1. Thermal analysis

Figure 4 shows the temperature field inside the solid for the *Reference* experiment and the temperature over time at the sample centre and at 3 mm of the rear side which is the approximate position of a thermocouple. The maximum temperature is 3265 K at the centre of the front face of the sample and approximatively 2814 K at the thermocouple positions. Discrepancies between recorded

12

and computed temperature can arise from several factors : (*i*) there can be errors in the thermocouple localisation, (*ii*) the materials (sample and holder) thermo-physical properties are temperature-dependent, (*iii*) the holder material made of *Calcarb*® also sublimes, resulting in an appreciable but difficulty measurable drop in thermal conductivity, and (*iv*) the time lag of the simulated temperature *vs.* the experimental one may arise from the initial power distribution, which is only considered as purely superficial, whereas the fibrous holder, being very porous, can bring power the interior of the setup more rapidly by radiation, not taken here into account. If we introduce this initial lag, then the simulated and experimental curve are in close agreement; therefore the temperature measurement is considered as validated. Moreover the temperature of the rear side of the sample holder does not exceed 1200 K which is acceptable in the experimental set-up.

Table 3 shows the velocity at the boundary layer edge u_e (m s^{-1}), the boundary layer size δ (mm), the temperature at 3 mm of the rear side of the sample T_{calc} and measured by thermocouple T_{exp}. T_{surf} is the surface temperature calculated by numerical analysis. It also presents the calculated recession r_{calc} (µm). We estimate the ablation velocity by dividing the mass loss rate by the material density, which means that the recession is assumed as homogeneous. The experimental temperature recording stopped approximatively at 26 s. At this point the measured value is 6.8 % higher than the calculated one (see table 3). This difference can be explained by the restrictive assumptions made in the simulation and by the accuracy on the thermocouple location. However, the steady-state surface temperature calculated by numerical heat transfer simulation is 3068 K, which is very close to the experimental value.

In figure 4b the steady state is close to be reached at the end of the experiment.
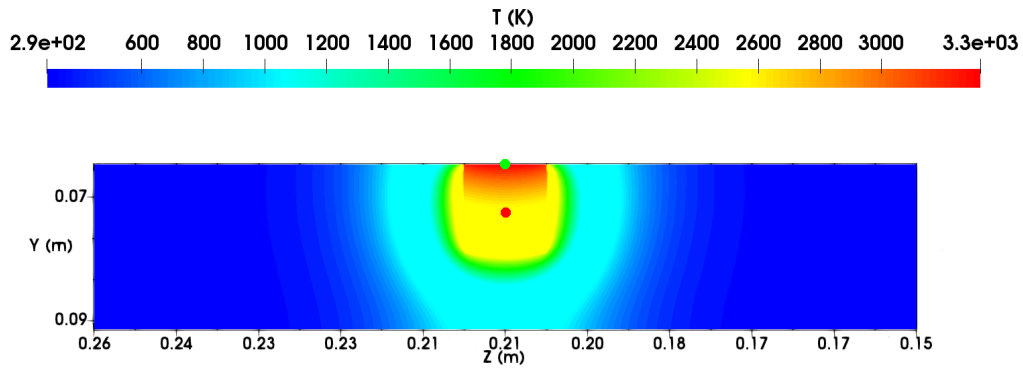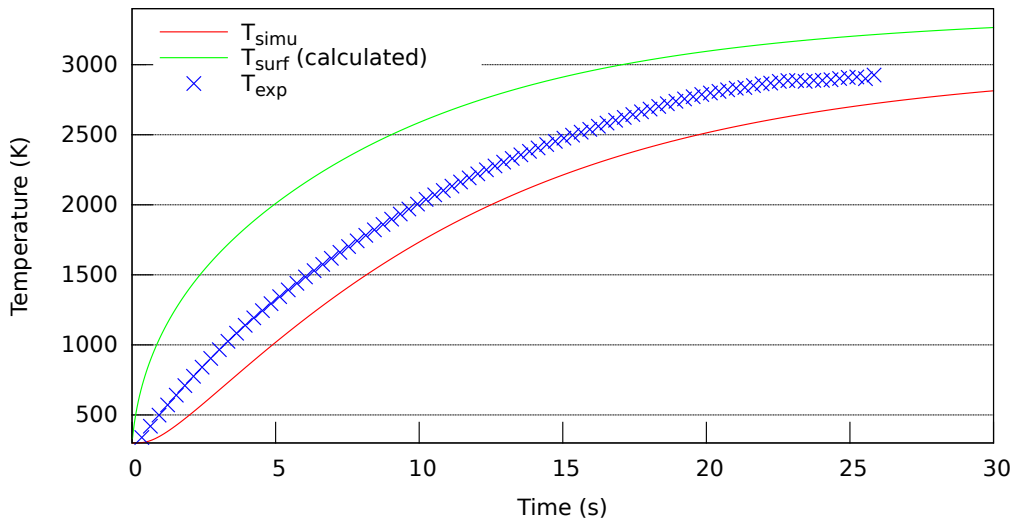
Figure 4: a) Temperature contours in the sample carrier assembly and b) plot of temperature over time at the surface centre and at a location 3 mm of the rear surface for a heat flux of $10\,\mathrm{MW\,m^{-2}}$ during 30 s

The maximum temperature reached is 2989 K for the simulation at $8\,\mathrm{MW\,m^{-2}}$ during 30 s and 2912 K for the 15 s test at $10\,\mathrm{MW\,m^{-2}}$ which are the most extreme cases. According to previous works, these values are sufficient to sublimate C_f/C composite [2] but they are only reached at the end of the experiment.

14

Sample	δ (mm)	u_e (m s^{-1})	T_{calc} (K)	T_{exp} (K)	T_{surf} (K)	r_{calc} (μm)
Reference	13.9	0.374	2814	2914	3265	43
Minimal sublimation	4.19	0.498	2560	-	2989	2.47
Mean pressure	6.61	0.506	2814	-	3265	43
High Pressure	4.19	0.521	2814	-	3265	42.9
Low flow rate	13.9	0.373	2814	-	3265	43
Transient	13.9	0.309	2213	-	2912	0.35

Table 3: Numerical boundary layer characterization and recession rate : boundary layer size δ, velocity parallel to the sample u_e, experimental temperature T_{exp}, thermocouple temperature T_{calc}, and surface temperature T_{surf} calculated by FE analysis, calculated total recession using equation (1) r_{calc}.

The ablated mass rate can be calculated using the Knudsen-Langmuir equation :

$$\dot{m}_{calc} = \sqrt{\frac{\bar{M}_C}{2\pi RT}} \sum_{i=1}^{5} \alpha_i \sqrt{i} \left(\bar{p_{C_i}}(T) - p_{C_i} \right) \tag{1}$$

where M_C is the molar mass of carbon, i represents the gaseous carbon chain length, α_i are Dalton coefficients [32], p_{C_i} are the partial pressures and $\bar{p}_{C_i}$ the equilibrium vapour pressure of the carbonaceous species C_i. Because of the argon flow, the carbon partial pressure above the sample can be considered as zero [33] and the equation can be solved using JANAF tables for equilibrium vapour pressure data [34]. The sample recession values presented in table 3 are calculated by integrating equation (1). Macroscopic ablation is difficult to quantify experimentally because the average recession height is very low compared to fibre bundle size (a few hundreds of μm). However, compared to the few micrometres of one fibre diameter, this recession height is sufficient for the observation of microscopic roughness features.
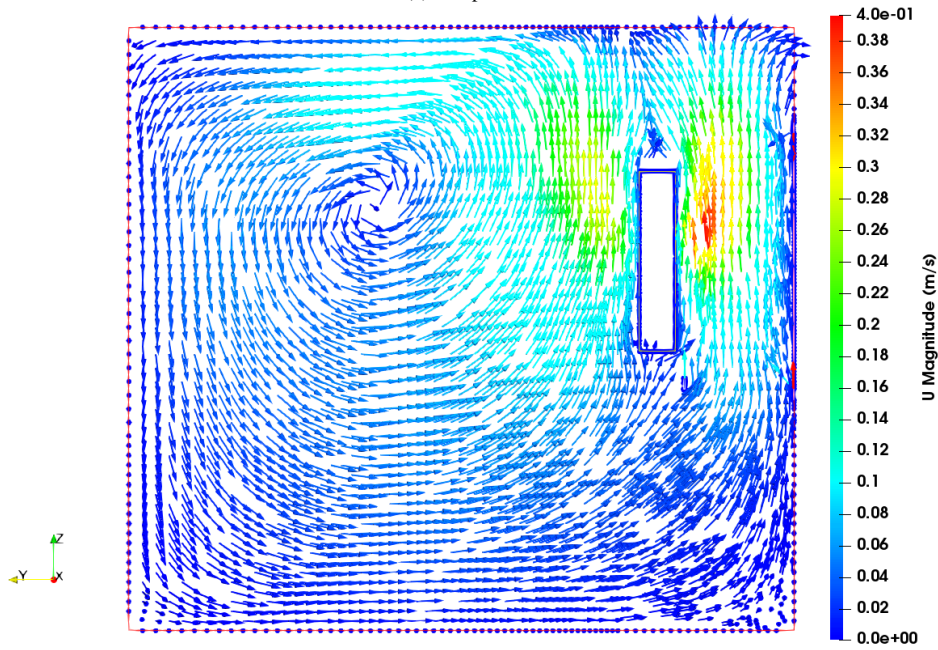
3.2.2. CFD simulation of the arc image furnace

Figure 5 presents plots of temperature contours and of velocity vectors for the *Reference* case. Heating of the gas is limited to a zone near the sample holder,

where the temperature of the fluid exceeds 3000 K. As it is clearly shown in figure 5b, the fluid is mainly driven by the stack effect, not by the injection device. Natural convection is the main source of fluid motion in this experiment.

Figure 6 is a plot of the velocity component parallel to the sample in front of its centre against the distance from the sample. Its magnitude is low ($< 1\ m\ s^{-1}$). So, the boundary layer size, defined as the distance between the maximum velocity abscissa and the sample surface, depends mainly on the static pressure and not on the injection flow rate.
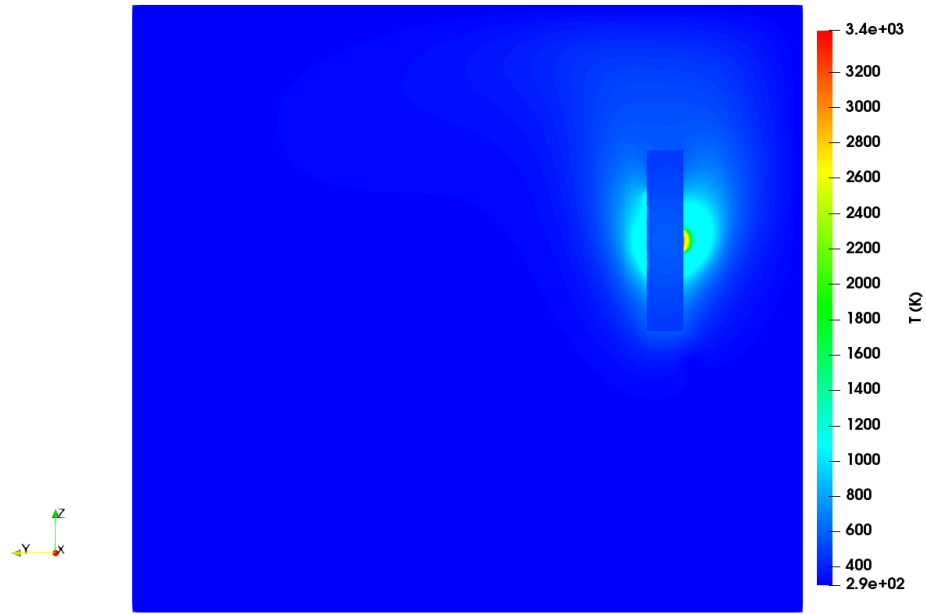
(a) Temperature

(b) Velocity magnitude

Figure 5: a) Temperature field and b) velocity vectors of a computation of the flow inside the arc image furnace for the *Reference* case
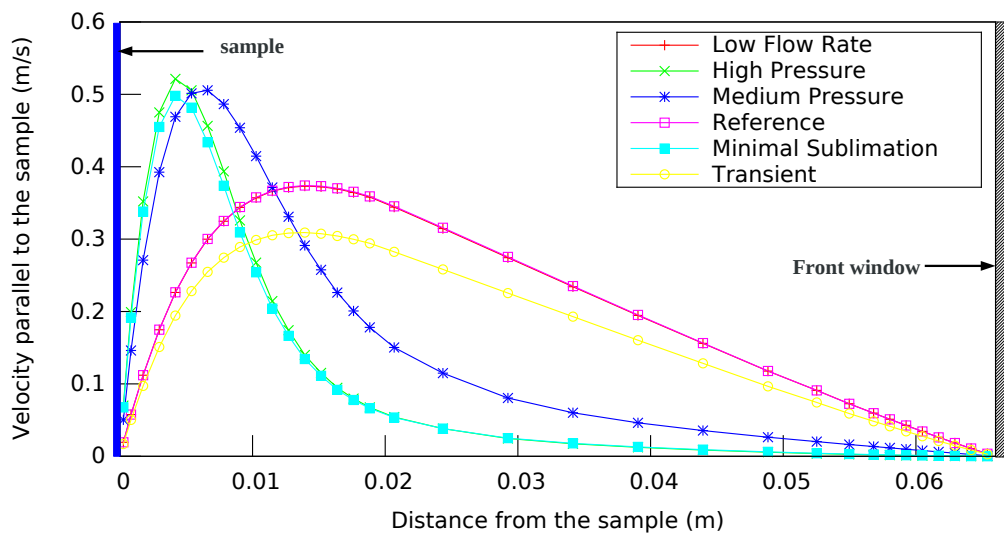
17

Figure 6: Velocity parallel to the sample along a normal segment starting from the sample centre and going to the front furnace window for the 30 s cases.

Summarizing, this simulation confirms that the injection device at the furnace window does not interact strongly with the main flow, which is mostly driven by natural convection. This ensures that the influence of the flow on surface ablation will be weak, which is desired for these experiments. The simulations also have confirmed that the outlet gases are not substantially heated.

3.3. Multiscale observation of ablated surface morphology

Figure 7 shows a 3D reconstructed picture of the surface of the sample after the sublimation test *Reference*. It is clearly seen that the vertical bundles have receded more quickly than the horizontal ones and the matrix pockets : the height difference is approximately 65 μm, larger than the estimated average recession height, 43 μm.
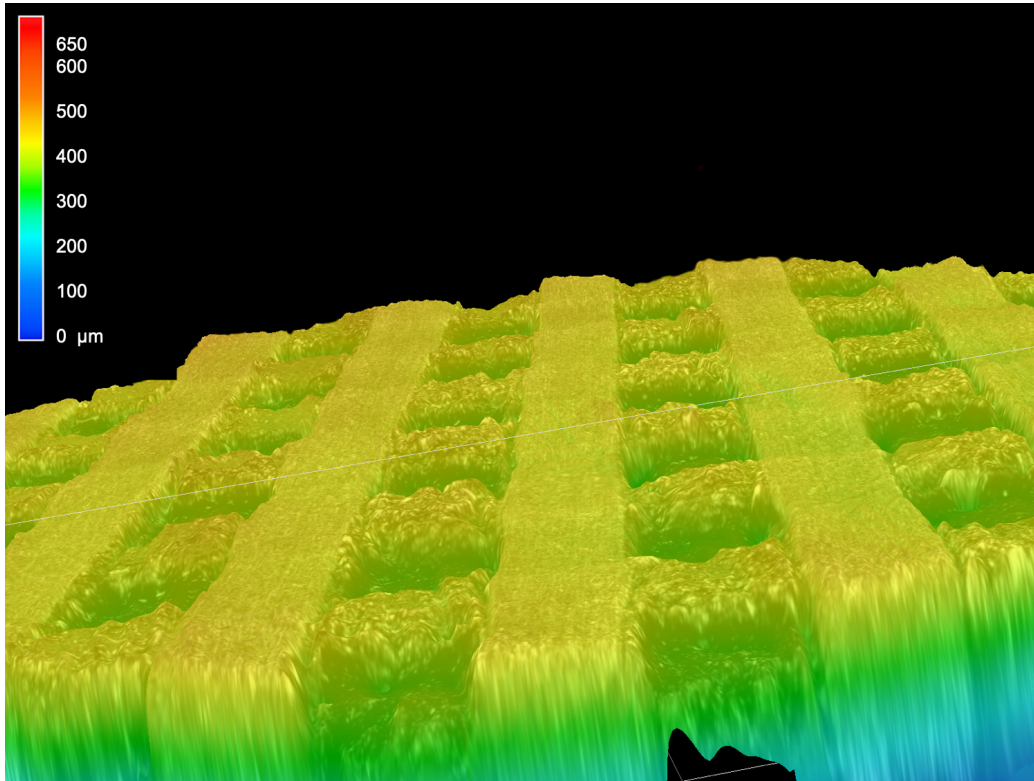
Figure 7: 3D microscopy reconstructed picture of the 3D C_f/C ablated under argon flow of an arc image furnace for the *Reference* test.

Figure 8a is an electron micrograph of the *Reference* sample surface. Cracks are visible between the different constituents of the 3D C_f/C as in an oxidation test [23]. They can result from ablation of the interface lying between fibre bundle and matrix, which is a frequently encountered phenomenon in the ablation of the 3D C_f/C [12, 14]. However, the contraction of the material during cooling is another plausible hypothesis to explain these grooves [23]. As seen in figure 8, the surfaces of the *Minimal sublimation* (b) and *Transient* (f) samples after test show almost the same cracks as the other ones (a,c,d,e), favouring the second phenomenon over the first one, though not eliminating it.

(a) *Reference*   (b) *Minimal sublimation*   (c) *Mean pressure*

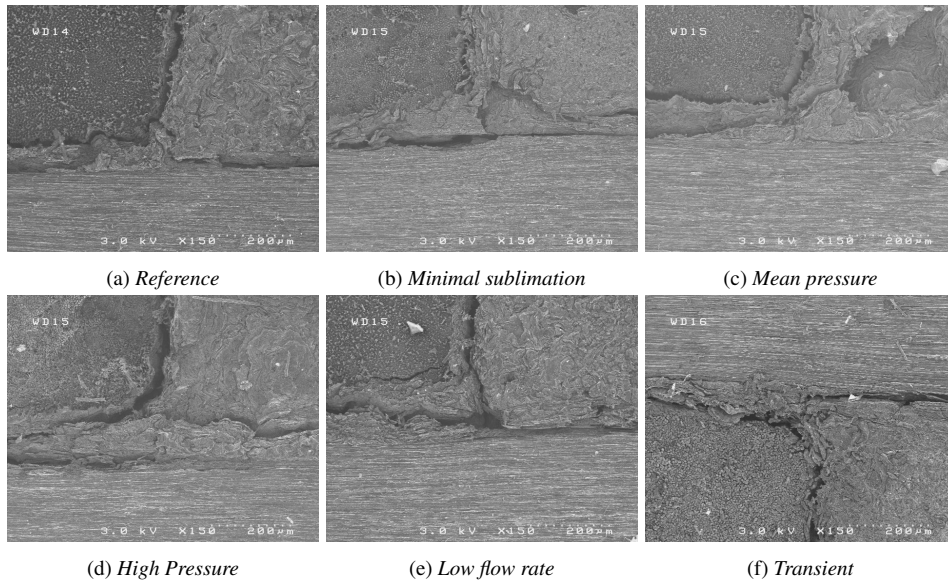(d) *High Pressure*   (e) *Low flow rate*   (f) *Transient*

Figure 8: SEM micrographs of surfaces after ablation tests. Experimental conditions are given in table 1.

Micrographs of bundles perpendicular to the surface after test are presented in figure 9. The intra-bundle matrix is less ablated than the fibres for all samples, as opposed to what occurs in oxidative conditions [12, 23]. The faster recession of the thin interface is already visible in figure 9f which has been obtained at the lowest temperature, with a minimal total recession. On the other micrographs, this interface is not visible any more because the fibres have receded much deeper than the matrix. The internal structure of the fibre, made of three concentric layers, is revealed, but not in the same way as in oxidation tests [12, 23]. Here, micrographs clearly show a more resistant core in the centre of the fibre, a skin is also evidence, but it is only hardly visible in figure 9f, indicating a poorly marked reactivity contrast with the intermediate region. Moreover, and as opposed to observations made in oxidation tests, the fibres display a mushy porous aspect. The core has smaller pores, with a lower pore density, as compared to the intermediate

21

region. On the other hand, the emerging matrix is not <mark>mushy,</mark> but rather under the form of stacked multilayer sheets. These are the most graphitized regions, which apparently better resist sublimation than the – probably less organised – carbon that embeds them. Comparing figures 9a, 9c and 9d, it is clear that increasing the total pressure decreases the amount of sublimation, as is well known [2]. On the other hand, comparing figs 9a and 9e, it is verified that changing the inlet argon flow rate does not change the local sublimation conditions on the sample.

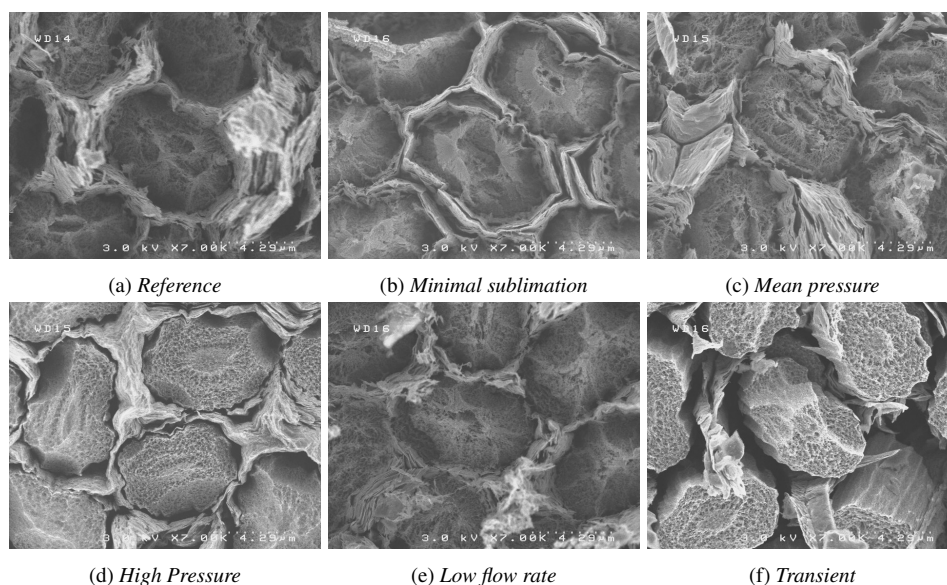|		
(a) *Reference*	(b) *Minimal sublimation*	(c) *Mean pressure*
(d) *High Pressure*	(e) *Low flow rate*	(f) *Transient*

Figure 9: SEM micrographs of fibres in bundles perpendicular to the surface after ablation test at an arc image furnace. Experimental conditions are given in table 1.

Figures 10a and 10b display the bundles parallel to the surface of the sample for *Transient* and *Reference* tests, respectively. These two cases have been selected because there are representative of the observed morphologies. Other samples have the same structures, more or less visible depending on the recession rate. At 15 s exposure, some notches can be seen on the fibres, which correspond to localised weak zones; the matrix seems striated in some parts. After 30 s, it

seems that no more fibres are visible on the surface, except some loose "wires" which are much thinner than the original fibres. This confirms the much larger tendency of the fibres to vaporise as compared to the matrix.
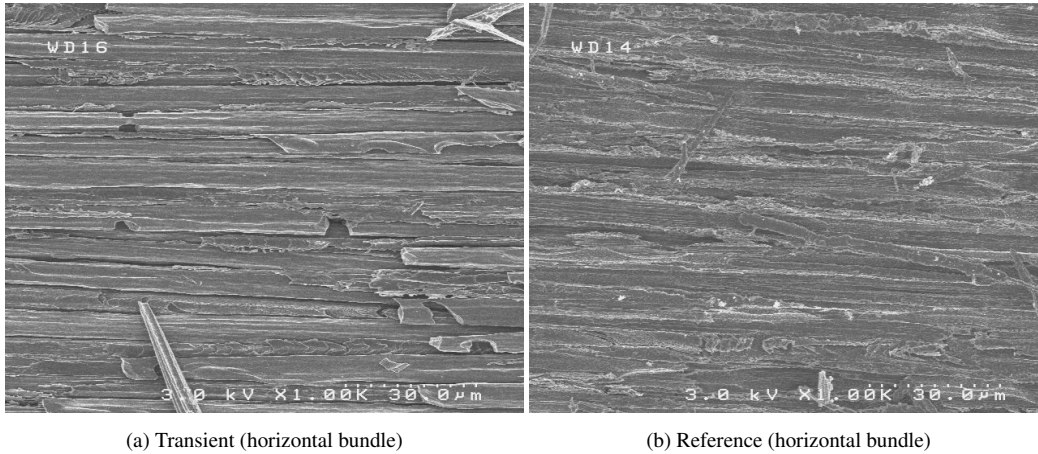

(a) Transient (horizontal bundle)   (b) Reference (horizontal bundle)

Figure 10: SEM micrographs of a horizontal bundle after 15 s and 30 s of exposure to a $10 \, \mathrm{MW \, m^{-2}}$ heat flux. Other experimental conditions are given in table 1 for *Transient* and *Reference* tests, respectively.

Figs. 11b and 11a are micrographs of the matrix pockets after after 15 s and 30 s of exposure to a $10 \, \mathrm{MW \, m^{-2}}$ heat flux (*Transient* and *Reference* tests, respectively). It can be seen that grains formed by stacked graphene sheets are progressively isolated from each other, revealing a composite structure of this matrix. Apparently, the sublimation rate is highly sensitive to the degree of organisation of carbon. If we consider that the matrix is some kind of composite material with well-organised grains embedded in a weaker matrix, then sublimations turns the matrix into a porous medium down to a certain depth.
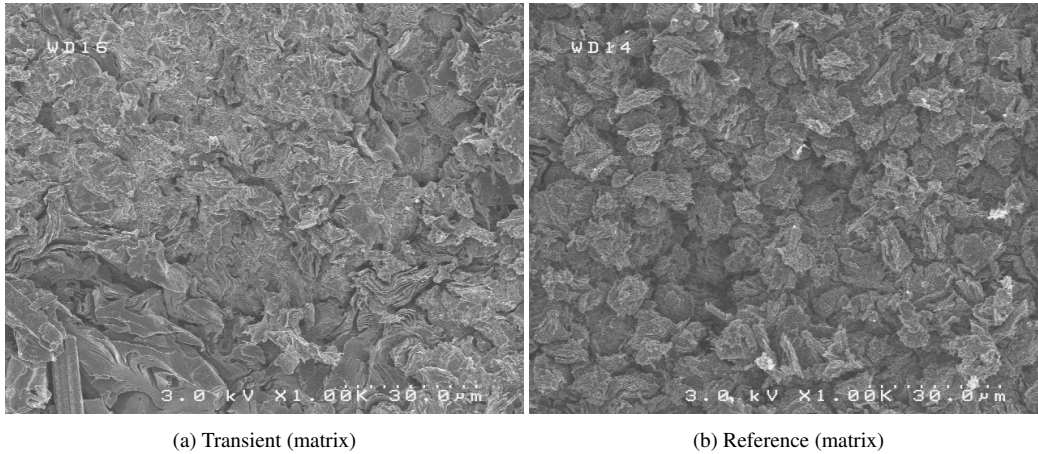
(a) Transient (matrix)　　　　　　　　(b) Reference (matrix)

Figure 11: SEM micrographs of the matrix after 15 s and 30 s of exposure to a $10\,\mathrm{MW\,m^{-2}}$ heat flux. Other experimental conditions are given in table 1 for *Transient* and *Reference* tests, respectively.

4. Discussion

4.1. Summary of the observations

Summarising all observations, it is clear that the matrix is less prone to sublimation than the fibres, as opposed to the case of oxidation for the same material [20, 23], confirming our preliminary work [12]. On the other hand, the presence of a weak phase between the major constituents, already been evidenced in many oxidation cases [13, 19, 35–37], seems to be confirmed here.

At microscopic scale, the fibre and the intra-bundle matrix are the main components of the 3D C_f/C, but a thin interface (less than 1 μm), made of a less organised matrix, separates these components. Contrary to the case of oxidation, the matrix is ablated at a rate lower or equal to the fibre. The highly ablated interface is not always visible: it is only seen in the lowest temperatures cases, especially the *Transient* case. Apparently, the interface reactivity is getting closer to the fibre one as temperature increases. The resulting morphologies are sketched in

Figure 12 : the fibre acquires a tip but is surrounded by a matrix "funnel", except in the case where the interface is not weaker than the fibre. In the latter situation, the fibre tip acquires a cone-shaped hole with its center more ablated than its periphery.
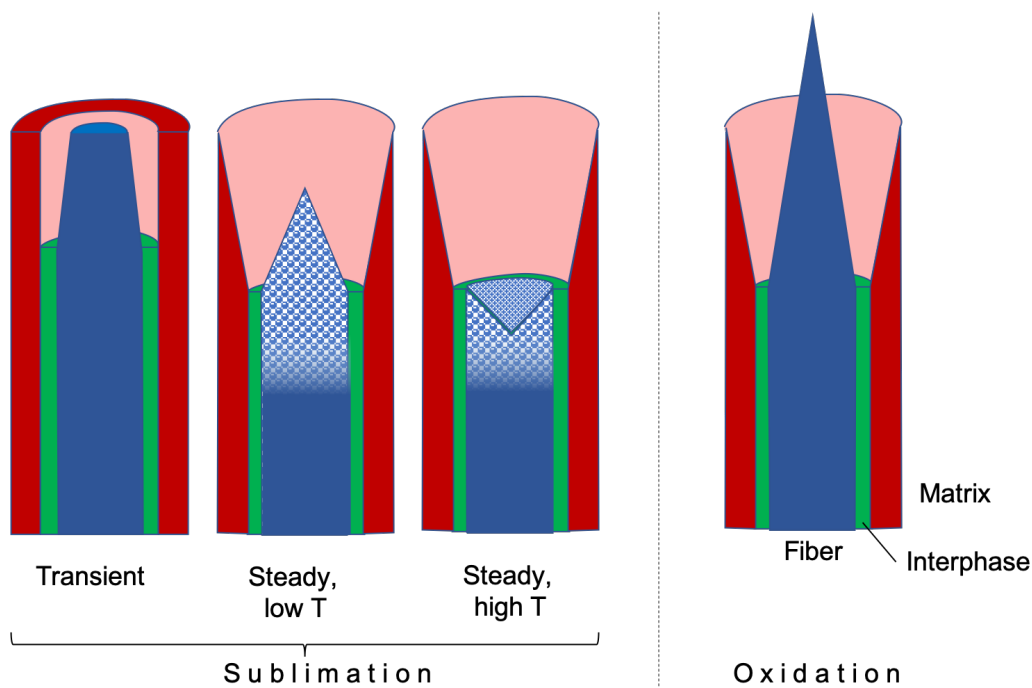

Figure 12: Schemes of the relative height between the fibre (blue), the interface (in green) and the intra bundle matrix (in red) for low temperature sublimation, high temperature sublimation and oxidation.

At the macro-scale, in a vertical bundle, the fibre tips are buried between matrix "walls" and the effective reactivity is driven by the fibres. On the other hand, in the horizontal bundles, the matrix offers some protection to the fibres, leading to a lower effective reactivity, almost similar to the matrix pockets. Therefore, at the macro-scale, the vertical bundles recede more than the horizontal ones and the

matrix pockets. One has to note that the short duration of the tests does not let enough time for a steady-state morphology to emerge: the total ablated height is much smaller than the section of the transverse bundles and matrix pockets.

Moreover, the comparison of samples ablated with different flow conditions and the results of the CFD study strongly indicate that the flow above the surface of the samples can be safely neglected, and that the recession is essentially limited by heterogeneous transfer, that is, by the intrinsic kinetics of carbon vaporisation, possibly in competition with diffusion from a small boundary layer above the surface.

In order to confirm these observations, some ablation simulations have been carried out.

4.2. Morphology simulations

We have used a home made ablation software named *AMA* (*Ablation Marche Aléatoire* in French) [16, 23, 29]. It is based on a Monte Carlo Random Walk algorithm for gas diffusion [38], with a sticking probability appropriately chosen for surface reaction [39] and a simplified marching cube discretisation of gas-solid interface [38, 40]. For the simulation, we have made two main hypotheses :

- (*i*) The transfer regime is limited by heterogeneous reactions, *i.e.* by the kinetics of solid vaporisation. Indeed, this is the regime in which the reactivity differences lead to the most marked roughness features [20].

- (*ii*) The fibre and matrix are chosen with a single reactivity for each.

- (*iii*) The fibre is supposed to be more reactive than the matrix, as suggested by the surface observations.

26

Constituent	Dimensions (pixels)	Reaction constant k (m s^{-1})	Reactivity ratio	Sherwood number $Sh = kL_{ref}/D$
		Fiber scale		
	Total domain size: $100 \times 100 \times 400$ ($//$) $100 \times 5 \times 600$ ($\perp$)			$L_{ref} =$ = Fiber radius
F/M Interface	1	$3.95 \cdot 10^{-2}$		$7.9 \cdot 10^{-2}$
Fiber	radius = 20	$1.72 \cdot 10^{-2}$	$11 : 5 : 1$	$3.5 \cdot 10^{-2}$
Matrix	min. thickness = 8	$3.51 \cdot 10^{-3}$		$7.0 \cdot 10^{-3}$
		Bundle scale		
	Total domain size : $100 \times 100 \times 150$			$L_{ref} =$ = 1/2 edge length
Interbundle Interface	1	$2.07 \cdot 10^{-2}$		$2.59 \cdot 10^{-2}$
Vert. bundle	edge length = 25	$9.06 \cdot 10^{-2}$	$8 : 3.5 : 1$	$1.13 \cdot 10^{-2}$
Horiz. bundle	edge length = 25	$2.66 \cdot 10^{-2}$		$3.33 \cdot 10^{-3}$

Table 4: Input parameters for the micro and macro-scale simulations.

- (*iv*) The thin interphase present between fibre and matrix is more reactive than both.

The reactivity ratios are 11:5:1 for interface, fibre and matrix respectively, in order to reproduce the observed features. The diffusion coefficient has been chosen so that the Sherwood number was low enough to ensure mass transfer limitations by heterogeneous kinetics. See Table 4 for a list of all chosen parameters. Indeed, it is known from theoretical considerations that in the reaction-limited regime, the height/radius ratio of an emerging fibre surrounded by a weak phase is equal to the weak phase/fibre reactivity ratio [20].

Figure 13 shows an SEM micrograph of the *Reference* sample after sublimation test, compared to a simulation of the recession with AMA. The simulated morphology obtained in stationary regime agrees qualitatively well with the exper-

imental results of the *Reference* case. Of course, more realism could be obtained if the fibre was attributed a core and a skin regions, but this simulation suffices to confirm the qualitative explanations mentioned in the preceding section.
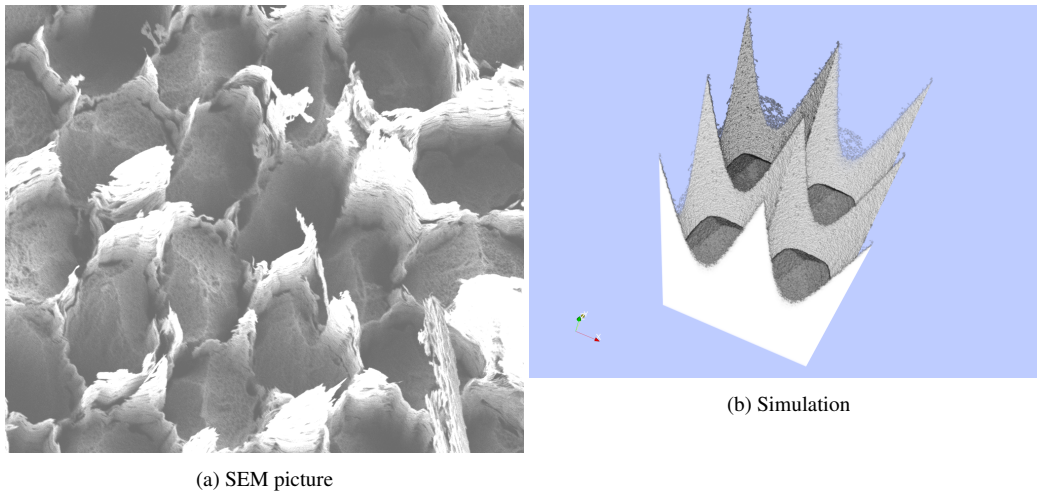

(a) SEM picture

(b) Simulation

Figure 13: a) SEM micrograph of a vertical fibres bundle of a 3D C_f/C ablated in an arc image furnace at $10\,\mathrm{MW\,m^{-2}}$ (From ref. [12], with permission) and b) simulation of the sublimation of a vertical fibre bundle with AMA software.

A simulation has been performed for the same fibre/interphase/matrix system oriented parallel to the average surface. Figure 14 shows that the effective reactivity of the transverse bundle is now rather close to the arithmetic average of the constituent reactivities. This confirms the partly protecting role of the matrix with respect to the weakest phases in this disposition, as opposed to the preceding one.
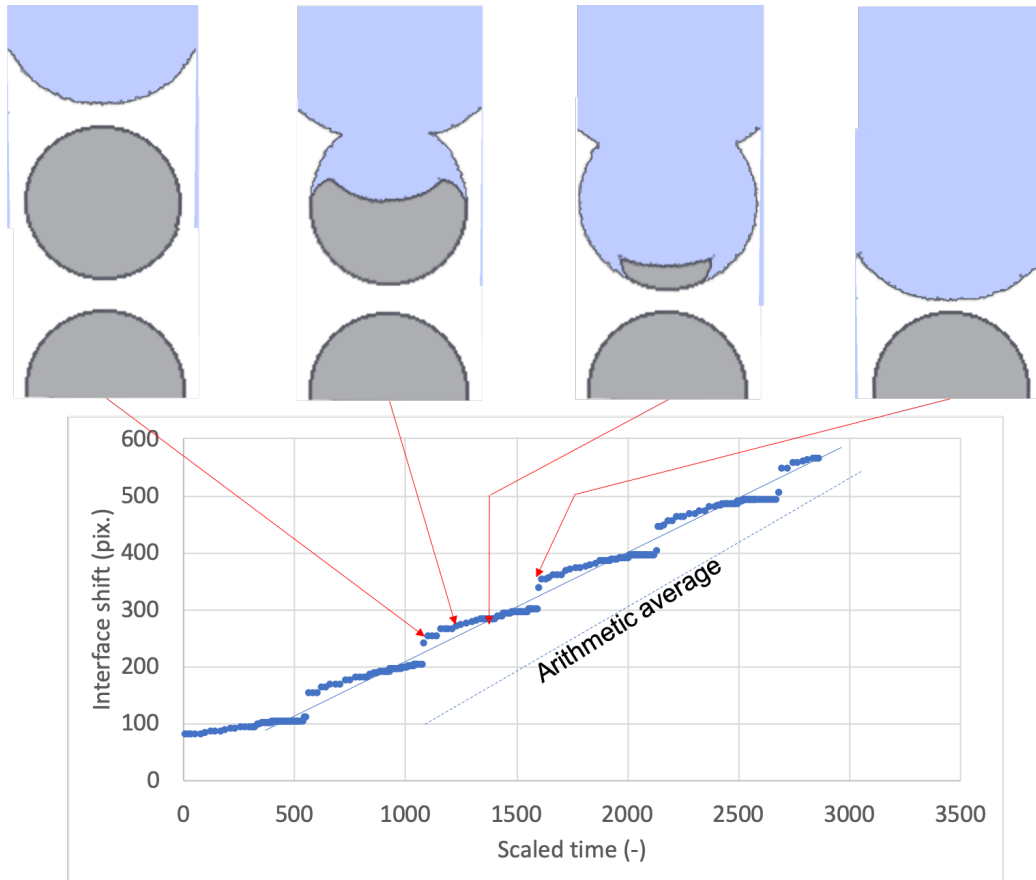
Figure 14: Simulation of the sublimation of a vertical fibre bundle with AMA software. The graph shows the evolution of the ablated height *vs.* time, and 4 snapshots of the surface morphology are given at chosen ablation time steps.

Simulations have also been run at large scale, and we have assumed that the vertical bundles are 3.5 times more reactive than the horizontal ones and the matrix pockets, with a weaker interphase, twice as weak as the vertical bundles. These ratios have been chosen according to the fact that the height difference between vertical and horizontal bundles is 65 µm while the average height loss is 43 µm. Figure 15 compares, for the *Reference* sample after sublimation test, the surface profile (fig. 7) to the simulation of the recession with AMA. Again, the simulated

morphology agrees qualitatively well with the experimental results. The contrasting behaviours of the vertical and horizontal bundles is accurately represented.
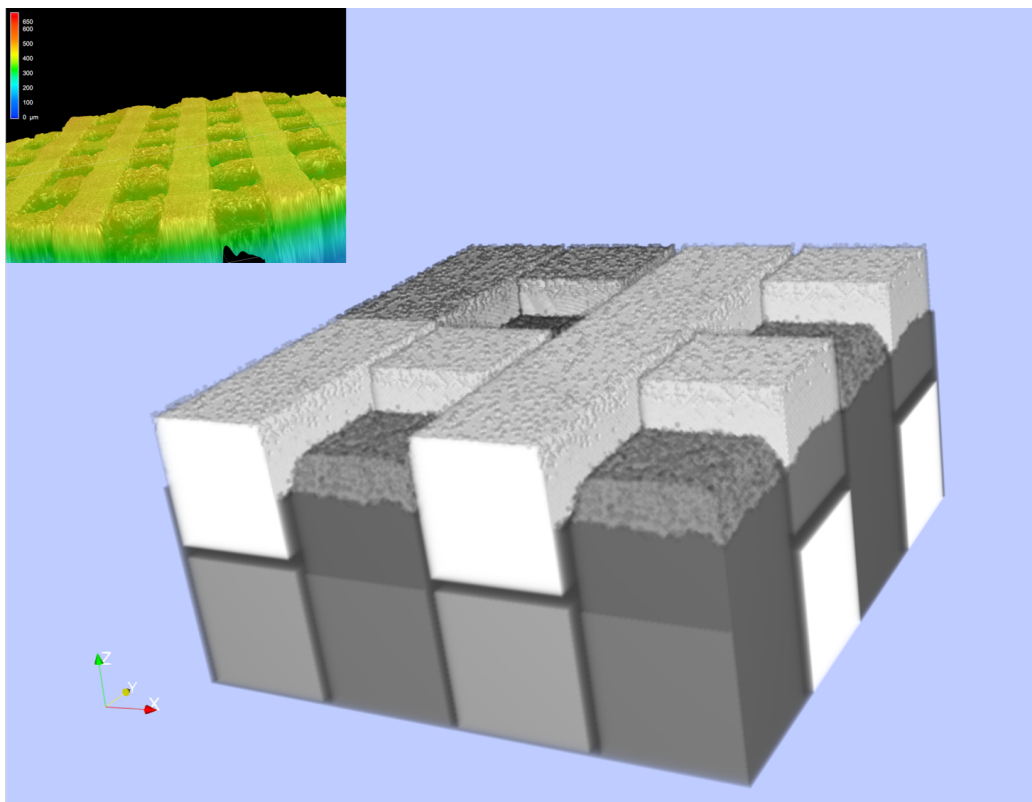

Figure 15: Simulation of the surface morphology obtained by sublimation with AMA software. The inset in the upper left corner shows the actual surface morphology.

An important point is that the observed features could be simulated without taking flow into account. So, as it has been supposed when setting up the furnace CFD model, and as suggested in the previous section from the comparison of the *Low Flow Rate* and *Reference* experiments, the surrounding flow does not play an important role in our tests.

4.3. Relations between carbon organisation and ablated surface features

If the matrix morphology is similar to the one observed in oxidation cases [23], the fibre has a very different appearance as compared to oxidation (compare *e.g.* Fig. 9 and Figs. 10 and 11 of [41]). Here it has a foamy, mushy structure, with pores of approximately tens of nanometers in size. The porous aspect of the ablated material suggests that the decomposition mechanism is different from that of oxidation. The pore dimensions are in line with the observed structure of the interior of a fibre (see Fig. 3d); this strongly suggests that the local degree of graphitization or at least of high anisotropy is an important factor for resistance to sublimation. So, sublimation seems to produce a volume ablation whereas oxidation produces clean surfaces. These observations agrees well with the choice made on some ablation models where oxidation is treated as a surface-based degradation whereas sublimation is a volume-based one [42–44].

PLOM measurements and HRTEM observations show that the intra bundle matrix is better organised than the fibres with longer graphene plans (section 3.1). This can be explained by the manufacturing process where the matrix is highly graphitized [8]. Moreover the matrix density is higher than the fibre due to the liquid crystal structure of the initial mesophasic pitch, combined to the numerous graphitization steps [1]. Both these facts can explain the resistance of the matrix during sublimation compared to the fibre. Again, it is seen here that a more organized carbon is much more resistant to the gasification process.

The same type of morphological evolution has been reported in a test submitting a needle-punched C/C composite to a nitrogen plasma at $\approx 25\,\mathrm{MW\,m^{-2}}$ [46]: vertical fibres acquired a needle shape but were buried inside matrix "funnels"; regions corresponding to needle-punching, oriented perpendicular to the surface,

have receded faster than the other parts of the composite surface. It cannot be ruled out that, due to the extreme temperatures of the test, sublimation has played a non-negligible, if not predominant role in the overall ablation. It is also possible that t dense carbons follows the same structure-reactivity relationships when exposed to nitrogen atoms as in the case of sublimation. Indeed, exposing vitreous carbon (containing randomly oriented graphitic domains) to beams containing N and/or O atoms results in rough surfaces on which the graphitic domains emerge from the less organised matrix [47], as is the case here.

5. Conclusion

Sublimation experiments on cylindrical samples of 3D C_f/C composites under argon have been carried out in an arc image furnace. Heat fluxes of $8\,\mathrm{MW\,m^{-2}}$ to $10\,\mathrm{MW\,m^{-2}}$ at test chamber pressures of 0.01 bar to 0.1 bar lead to a surface temperature range of 2919 K to 3265 K. The temperature inside the sample holder assembly and the flow field were reconstructed using CFD simulations. Recession velocity values were then estimated from these CFD calculations and literature data and were found very low, confirming direct observations. The nanotexture of the virgin composite was studied using HRTEM and PLOM analyses. SEM micrographs of all cases were taken and the previously described "inverse" behaviour of sublimation as compared to oxidation was found at micro- and macro-scale. 3D digital microscopy was used to obtain three-dimensional view of the ablated samples at macroscopic scale.
From HRTEM and PLOM analyses it was observed that the highly graphitized matrix is more organised than the fibres. This can explained the observations made after sublimation tests. The more anisotropic carbon is less resistant to sublimation process. This is qualitatively confirmed by numerical simulations by

32

AMA software.

The fibres have been found to acquire a porous morphology under sublimation, which can be understood on the following grounds : (*i*) the fibres contain small well-organised domains embedded in a less organised "binding carbon", (*ii*) the sublimation rate is strongly related to the local degree of carbon organisation.

In order to be more representative of atmospheric entry conditions the influence of high speed flow have to be explored. This can be done with experimental set-ups allowing higher sublimation rate or longer sample exposures and is the objective of future work. Moreover testing individual 3D C_f/C components in sublimation conditions, as has already been done for oxidation [41, 45] is necessary to feed microscopic sublimation models and to improve accuracy of TPS ablation prediction.

Acknowledgements

References

[1] G. Savage. *Carbon/Carbon composites*. Springer Netherlands, 1993. ISBN: 0-412-36150-7.

[2] G. Duffa. *Ablative Thermal Protection systems modeling*. AIAA Education Series. AIAA, New York, 2013. DOI:10.2514/4.101717

[3] J. Couzi, J. de Winne, and B. Leroy. Improvements in ablation predictions for reentry vehicle nosetip. In :R.A. Harris, editor, *Proceedings of the 3ʳᵈ*

European Symposium on Aerothermodynamics for space vehicles, volume SP-426 of *ESA Conf. Procs.*, pages 493–499, Noordwijk, The Netherlands, 1998. ISBN: 9-290-92704-6.

[4] J. Lachaud. *Modélisation physico-chimique de l'ablation de matériaux composites en carbone*. PhD thesis, University of Bordeaux, 2006. http://theses.fr/2006BOR13291

[5] K. K. Kuo and S. T. Keswani. A comprehensive theoretical model for carbon-carbon composite nozzle recession. *Combustion Science and Technology*, 42(3-4):145–164, 1985. DOI:10.1080/00102208508960374

[6] V. Borie, J. Brulard, and G. Lengellé. Aerothermochemical analysis of carbon-carbon nozzle regression in solid-propellant rocket motors. *Journal of Propulsion and Power*, 5(6):665–673, 1989. DOI:10.2514/3.23204

[7] D. Boury and L. Filipuzzi. SEPCARB materials for solid rocket booster nozzle components. Procs. 37th AIAA/ASME/SAE/ASEE Joint Propulsion Conference and Exhibit. *AIAA Paper* 2001-3438, 2001. DOI:10.2514/6.2001-3438

[8] E. Fitzer and Lalit M. Manocha. *Carbon Reinforcements and Carbon/Carbon Composites*. Springer, Berlin Heidelberg, 1998. DOI:10.1007/978-3-642-58745-0

[9] S. Pestchanyi, V. Safronov, and I. Landman. Estimation of carbon fibre composites as ITER divertor armour. *Journal of Nuclear Materials*, 329-333:697–701, 2004. DOI:10.1016/j.jnucmat.2004.04.189

[10] D. M. Duffy. Fusion power materials. *Advanced Materials and Processes*, 168(7):15–18, 2010. https://www.asminternational.org/news/magazines/amp/-/journal_content/56/10192/AMP16807P15/PERIODICAL-ARTICLE

[11] G. L. Vignoles, A. Turchi, D. Bianchi, P. Blaineau, X. Lamboley, D. Le Quang Huy, C. Levet, O. Caty, and O. Chazot. Ablative and catalytic behavior of carbon-based porous thermal protection materials in nitrogen plasmas. *Carbon*, 134:376–390, 2018. DOI:10.1016/j.carbon.2018.03.087

[12] G. L. Vignoles, J. Lachaud, and Y. Aspa. Environmental effects: Ablation of *C/C* materials – surface dynamics and effective reactivity. In : Narottam P. Bansal and J. Lamon, editors, *Ceramic Matrix Composites: Materials, Modeling and Technology*, chapter 12, pages 353 – 384. Wiley & American Ceramic Society, Hoboken, NJ, 2014. DOI:10.1002/9781118832998.ch12

[13] D.-W. Cho and B.-I. Yoon. Microstructural interpretation of the effect of various matrices on the ablation properties of carbon-fiber-reinforced composites. *Composites Science and Technology*, 61(2):271–280, 2001. DOI:10.1016/S0266-3538(00)00212-8

[14] J. Lachaud, G. L. Vignoles, J.-M. Goyhénèche, and J.-F. Epherre. Ablation in Carbon/Carbon Composites: Microscopic Observations and 3D Numerical Simulation of Surface Roughness Evolution. In :M. Affatigato, editor, *Interfaces in Heterogeneous Ceramic Systems: Ceramic Transactions Series, Volume 191*, pages 147–160. John Wiley & Sons, Ltd, 2006. DOI:10.1002/9781118144084.ch12

[15] K.-Z. Li, X.-T. Shen, H.-J. Li, S.-Y. Zhang, T. Feng, and L.-L. Zhang. Ab-

lation of the carbon/carbon composite nozzle-throats in a small solid rocket motor. *Carbon*, 49(4):1208–1215, 2011. DOI:10.1016/j.carbon.2010.11.037

[16] G. L. Vignoles, J. Lachaud, Y. Aspa, and J.-M. Goyhénèche. Ablation of carbon-based materials: Multiscale roughness modelling. *Composites Science and Technology*, 69(9):1470–1477, 2009. DOI:10.1016/j.compscitech.2008.09.019

[17] R. G. Batt and H. H. Legner. A Review of Roughness-Induced Nosetip Transition. *AIAA Journal*, 21(1):7–22, 1983. DOI:10.2514/3.60102

[18] D. C. Reda. Correlation of Nosetip Boundary Layer Transition Data measured in Ballistic Range Experiments. *AIAA Journal* 19(3): 329-339, 1981. DOI:10.2514/3.50952

[19] J.-C. Han, X.-D. He, and S.-Y. Du. Oxidation and ablation of 3D carbon-carbon composite at up to 3000 °C. *Carbon*, 33(4):473–478, 1995. DOI:10.1016/0008-6223(94)00172-V

[20] J. Lachaud, Y. Aspa, and G. L. Vignoles. Analytical modeling of the steady state ablation of a 3D C/C composite. *International Journal of Heat and Mass Transfer*, 51(9):2614–2627, 2008. DOI:10.1016/j.ijheatmasstransfer.2008.01.008

[21] B. Chen, L.-T. Zhang, L.-F. Cheng, and X.-G. Luan. Erosion resistance of needled carbon/carbon composites exposed to solid rocket motor plumes. *Carbon*, 47(6):1474–1479, 2009. DOI:10.1016/j.carbon.2009.01.040

[22] B. Helber, O. Chazot, A. Hubin, and T. E. Magin. Microstructure and gas-surface interaction studies of a low-density carbon-bonded

carbon fiber composite in atmospheric entry plasmas. *Composites Part A: Applied Science and Manufacturing*, 72:96–107, 2015. DOI:10.1016/j.compositesa.2015.02.004

[23] C. Levet, B. Helber, J. Couzi, J. Mathiaud, J.-B. Gouriet, O. Chazot, and G. L. Vignoles. Microstructure and gas-surface interaction studies of a 3D carbon/carbon composite in atmospheric entry plasma. *Carbon*, 114:84–97, 2017. DOI:10.1016/j.carbon.2016.11.054

[24] L. M. Gilbert and S. M. Scala. Sublimation of graphite at hypersonic speeds. *AIAA Journal*, 3(9):1635–1644, 1965. DOI:10.2514/3.3220

[25] N. S. Diaconis, M. J. Engel, and J. W. Metzger. Oxidation and sublimation of graphite in simulated re-entry environments. *AIAA Journal*, 5(3):451–460, 1967. DOI:10.2514/3.4001

[26] J. H. Lundell and R. R. Dickey. Ablation of Graphitic Materials in the Sublimation Regime. *AIAA Journal*, 13(8):1079–1085, 1975. DOI:10.2514/3.60505

[27] S. Farhan, R. Wang, K.-Z. Li, and C. Wang. Sublimation and oxidation zone ablation behavior of carbon/carbon composites. *Ceramics International*, 41(10, Part A):13751–13758, 2015. DOI:10.1016/j.ceramint.2015.08.043

[28] V. Ducamp. *Transferts thermiques dans un matériau composite carbone résine*. PhD thesis, University Bordeaux 1, 2002. http://theses.fr/2002BOR12505

[29] J. Lachaud and G. L. Vignoles. A Brownian motion technique

to simulate gasification and its application to C/C composite ablation. *Computational Materials Science*, 44(4):1034–1041, 2009. DOI:10.1016/j.commatsci.2008.07.015

[30] A. P. Gillard, G. Couégnat, S. Chupin, and G. L. Vignoles. Modeling of the non-linear mechanical and thermomechanical behavior of 3D carbon/carbon composites based on internal interfaces. *Carbon*, 154:178–191, 2019. DOI:10.1016/j.carbon.2019.07.101

[31] A. P. Gillard, G. Couégnat, O. Caty, A. Allemand, P. Weisbecker, and G. L. Vignoles. A quantitative, space-resolved method for optical anisotropy estimation in bulk carbons. *Carbon*, 91:423–435, 2015. DOI:10.1016/j.carbon.2015.05.005

[32] T. A. Dolton, H. E. Goldstein, and R. E. Maurer. Thermodynamic performances of carbon in hyperthermal environments. In :J. T. Bevans, Ed., *Thermal Design Principles of Spacecraft and Entry Bodies*, Academic Press, 1969, pages 169-201. DOI:10.2514/5.9781600864957.0169.0201

[33] T. Paulmier, M. Balat-Pichelin, D. Le Quéau, R. Berjoan, and J.-F. Robert. Physico-chemical behavior of carbon materials under high temperature and ion irradiation. *Applied Surface Science*, 180(3):227–245, 2001. DOI:10.1016/S0169-4332(01)00351-8

[34] M. W. Chase, J. R. Davies, J. R. Downey, D. J. Frurip, R. A. McDonald, and A. N. Syverud. JANAF Thermodynamical Tables, 3rd edition. *Journal of Physical Chemical Reference Data* 14, 1985. DOI:10.18434/T42S31

[35] E. Duvivier. *Cinétique d'oxydation d'un composite carbone/carbone et influence sur le comportement mécanique*. PhD thesis, University Bordeaux I, 1997. http://theses.fr/1997BOR10539

[36] E. Duvivier, R. Naslain, R. Pailler, X. Bourrat, and S. Labruquère. The role of interfaces in the oxidation of 3D-carbon/carbon composites. In :*Procs. 26th Annual Conference on Composites, Advanced Ceramics, Materials, and Structures: A: Ceramic Engineering and Science Proceedings*, 23(3):287 - 294. John Wiley & Sons, New York, 2002. DOI:10.1002/9780470294741.ch33

[37] Y.-J. Lee and H.-J. Joo. Investigation on ablation behavior of CFRC composites prepared at different pressure. *Composites Part A: Applied Science and Manufacturing*, 35(11):1285–1290, 2004. DOI:10.1016/j.compositesa.2004.03.024

[38] G. L. Vignoles. Modelling binary, Knudsen, and transition regime diffusion inside complex porous media. *Journal de Physique IV France*, 5(C5):C5-159–C5-166, 1995. DOI:10.1051/jphyscol:1995517

[39] J. C. Ferguson, F. Panerai, J. Lachaud, A. Martin, S. C.C. Bailey, and N. N. Mansour. Modeling the oxidation of low-density carbon fiber material based on micro-tomography. *Carbon*, 96:57–65, 2016. DOI:10.1016/j.carbon.2015.08.113

[40] G. L. Vignoles, M. Donias, C. Mulat, C. Germain, and J.-F. Delesse. Simplified marching cubes: An efficient discretization scheme for simulations

of deposition/ablation in complex media. *Computational Materials Science*, 50(3):893–902, 2011. DOI:10.1016/j.commatsci.2010.10.027

[41] J. Lachaud, Y. Aspa, and G. L. Vignoles. Analytical modeling of the transient ablation of a 3D C/C composite. *International Journal of Heat and Mass Transfer*, 115:1150–1165, 2017. DOI:10.1016/j.ijheatmasstransfer.2017.06.130

[42] J. Marschall and M. McLean. Finite-Rate Surface Chemistry Model, I: Formulation and Reaction System Examples. In :*Procs. 42nd AIAA Thermophysics Conference*, *AIAA Paper* 2011-3783, 2011. DOI:10.2514/6.2011-3783

[43] E. D. Farbar, H. Alkandry, J. Wiebenga, and I. D. Boyd. Simulation of Ablating Hypersonic Vehicles with Finite-Rate Surface Chemistry. In :*Procs. 11th AIAA/ASME Joint Thermophysics and Heat Transfer Conference*. *AIAA Paper* 2014-2124, 2014. DOI:10.2514/6.2014-2124

[44] C. Alba, R. B. Greendyke, and J. Marschall. Influence of Carbon Nitridation in a Nonequilibrium Finite-Rate Ablation Model. In :AIAA, editor, *Procs. 53rd AIAA Aerospace Sciences Meeting*, *AIAA Paper* 2015-1453, 2015. DOI:10.2514/6.2015-1453

[45] J. Lachaud, N. Bertrand, G. L. Vignoles, G. Bourget, F. Rebillat, and P. Weisbecker. A theoretical/experimental approach to the intrinsic oxidation reactivities of C/C composites and of their components. *Carbon*, 45(14):2768–2776, 2007. DOI:10.1016/j.carbon.2007.09.034

[46] X.-T. Shen, Z.-Q. Shi, Z.-G Zhao, X. Wang. C.-Y. Li, J.-F. Huang, K.-Z. Li, and G. Liu, Study of the ablation of a carbon/carbon composite at ≈ 25 MW/m^2 with a nitrogen plasma torch. *Journal of the European Ceramic Society* , 40(15):5085-5093, 2020. DOI:10.1016/j.jeurceramsoc.2020.06.075

[47] V.J. Murray, P. Recio, A. Caracciolo, C. Miossec, N. Balucani, P. Casavecchia, and T.K. Minton. Oxidation and nitridation of vitreous carbon at high temperatures. *Carbon*, 167:388–402, 2020. DOI: 10.1016/j.carbon.2020.05.076